Enhanced Land Vehicle Positioning in Challenging GNSS Urban Environments Utilizing Automotive Radars

Marwan A. Rashed, Haidy Elghamrawy, *Member, IEEE*, Mohamed Elhabiby, Michael J. Korenberg, and Aboelmagd Noureldin, *Senior Member, IEEE*

Abstract— **Positioning services for land vehicle navigation have long relied on global navigation satellite systems (GNSS); however, GNSS cannot maintain an accurate position while travelling under bridges, around tall buildings and under tree canopies due to signal blockage or multipath. Integration with the onboard motion sensors can bridge the positioning solution for a short duration but cannot sustain adequate positioning performance during extended GNSS outages. The proposed research overcomes the limitations of current positioning technologies for land vehicles by integrating a GNSS receiver, onboard motion sensors, and an electronic scanning radar (ESR) used in present land vehicles for adaptive cruise control. A new ESR-based static object detection method is developed using newly designed criteria to estimate the forward velocity. We also propose a radar odometry method to obtain the vehicle position based on the radar scans. Integration with onboard motion sensors based on Extended Kalman filtering (EKF) is designed and realized to achieve accurate positioning in degraded vision and challenging GNSS environments. The proposed multi-sensor positioning solution is examined using several road test trajectories in challenging urban environments in Toronto. It shows RMS error as low as 3 m over more than 90% of the traveled distance.**

Index Terms—**Positioning, GNSS, Inertial Navigation System (INS), Automotive radars, ESR, Static object detection, Median Absolute Deviation (MAD), EKF.**

Marwan Rashed is with the Department of Electrical and Computer Engineering, Queen's University, Kingston, ON K7L 3N6, Canada.

Haidy Elghamrawy is with the Department of Electrical and Computer Engineering, Royal Military College of Canada, Kingston, ON K7K 7B4, Canada (e-mail: haidy.elghamrawy@queensu.ca).

Mohamed Elhabiby is with the Faculty of Engineering, Ain Shams University, 1 El Sarayat St.، ABBASSEYA, El Weili, Cairo Governorate 11535, Egypt.

Michael Korenberg is with the Department of Electrical and Computer Engineering, Queen's University, Kingston, ON K7L 3N6, Canada.

Aboelmagd Noureldin is with the Department of Electrical and Computer Engineering, Royal Military College of Canada, Kingston, ON K7K 7B4, Canada, and also with School of Computing, Queen's University, Kingston, ON K7L 3N6, Canada.

Color versions of one or more of the figures in this article are available online at http://ieeexplore.ieee.org

I. INTRODUCTION

Positioning has played a vital role in the vehicular industry for decades. However, positioning importance increased as the advancements in vehicular technology led to the autonomous vehicles (AV) era. Consequently, the demand for accurate positioning systems has experienced unprecedented ubiquity [1-2]. Positioning accompanies several sub-tasks, such as static obstacle mapping, moving obstacles detection, recognition, and avoidance, to form the perception task in the vehicle autonomy architecture [3].

Land vehicle positioning has long relied on GNSS, which cannot maintain an accurate vehicle position under bridges, around tall buildings and under tree canopies due to signal blockage or multipath [4-5]. Integration with the onboard inertial sensors and speedometers can bridge GNSS outages for only a short period of time [6]. Both cameras and LiDAR may fail to provide accurate positioning when operating under challenging weather conditions of snow, heavy rain or fog [7-8]. It is necessary to fill this critical gap by devising a weather-independent solution integrating electronic scanning radars (ESR) utilized for adaptive cruise control as an alternative to Light Detection and Ranging (LiDAR) and cameras to detect objects and provide range estimation [9].

A. Problem Statement

Future land vehicles will include a batch of sensors to understand the perceptual semantics in the surrounding world. LiDAR, Monocular/Stereo vision Cameras, and **RA**dio **D**etection And **R**anging (Radar) sensors are state-of-the-art equipment used in such systems [3]. Machine vision approaches based on LiDAR and Cameras have been explored for several autonomous vehicle purposes, including positioning and navigation [10-11]. However, the feasibility of applying these methods in real-time in land vehicles and passenger cars is limited due to the lack of adequate processing power. Although LiDAR is a high-resolution mapping sensor with the capability of detecting a vast number of objects in one scan, it causes severe design restrictions and requires sophisticated real-time computations [12-14]. Similarly, visual odometry (VO) performs poorly in the urban environment in case of shadowing from high-rise buildings and at night or in an indoor environment (e.g., parking garages) due to the lack of adequate light conditions [15-17]. Besides, both sensors are not included in all levels of driving autonomy, and most status quo vehicles do not utilize LiDAR

due to their relatively high cost at present [18]. The implementation of LiDAR technology on land vehicles is currently in progress.

On the contrary, radars are deployed into land vehicles for a long time with an established stable original equipment manufacturer (OEM) market, which led to a well-defined cheap cost and optimized computational capabilities for land vehicles specifically. Consequentially, automotive radars come in a wide range of forms, mounting locations, and applications with object detection and tracking being in the center of uses. As a result, the introduced techniques in this work can be deployed instantly and widely. Moreover, automotive radars are presently used in a wide range of cars for adaptive cruise control purposes [19]. The radar signal processing does not require complex computational algorithms, powerful hardware, or high utilization costs compared to LiDAR [20][14]. Moreover, radar accomplishes the same performance in all weather conditions (e.g., snow, rain, and fog) where LiDAR and VO may fail since radar signal is not affected by a lack of light or any non-metallic obstacles [21]. In conclusion, different sensors have their own points of strengths and weaknesses based on how they are adopted in a sensor fusion scheme. Radar is well-known for its resilience when it comes to challenging circumstances in the surroundings such as rain and snow. Additionally, radars are widely used for range and speed detection in different industrial fields. Nevertheless, LiDAR suffers from environmental difficulties like cameras and is mainly used in mapping with no Doppler velocity information being captured; it still has a better description of the vehicle's surrounding scene with a higher density of points. In this paper, we are utilizing radars' superiority in velocity detection to form a more robust positioning algorithm. Hence, it is believed that radar would outperform other sensors when it comes to a velocity update in a loosely coupled EKF.

B. Motivation

Recently, most high, and middle-class land vehicles have been equipped with automotive radars. Automotive radars utilize various technologies such as single-antenna and an array of antennas radar. Both technologies detect the ranges between the ego-vehicle and the surrounding objects. However, single antenna radars are limited to range detection, while multiple antenna radars can detect bearing angles too. This feature degrades the single antenna radar in understanding the perceptual semantics of the environment and widens the functionalities based on multiple antenna radars. A specific type of multiple antenna radar called ESR is mostly used in land vehicles [22]. ESR is mainly utilized in Advanced Driver-Assistance Systems (ADAS), where it performs object detection and avoidance, besides the Adaptive Cruise Control (ACC) [23]. There are several advantages of using ESR in positioning algorithms. The main one is the ability to determine the object's range, radial velocity, and bearing angle [24]. These features can lead to adequate discrimination between static and moving objects. Hence, static objects can be extracted from the ESR scans and used in robust velocity estimation. It is also a practical approach that matches the current status of the vehicular industry's

dependency on ESRs. Therefore, designing a multi-sensor fusion system based on integrating ESR with both GNSS and reduced inertial sensor system (RISS) can enhance the performance of the overall positioning solution.

C. Contributions

This paper aims to develop a continuous, reliable, and accurate positioning solution with a consistent level of accuracy in challenging and fully denied GNSS urban environments. To achieve this target, the specific goals are as follows:

1) Design detection criteria and employ several outlier rejection methods to develop and implement static object detectors. The detected objects are utilized for velocity estimation and vehicle positioning.
2) Design and implement an ESR-based positioning method that depends on the estimated vehicle's velocity to provide a standalone positioning solution.
3) Design and implement a practical multi-sensor positioning system based on a single ESR.
4) Design an Extended Kalman Filter (EKF) loosely coupled integration between an ESR, RISS, and GNSS to achieve accurate positioning seamlessly for all environments with an intelligent switching mechanism.

The main contribution of this paper is to develop a multi-sensor integration method for car navigation that does not only rely on the integration of inertial sensors with GNSS but also on the scans from a single ESR mounted on the front bumper of the vehicle. This sensor is used in present cars for adaptive cruise control. However, it is used in this research to provide complementary information about the vehicle position and heading that can be integrated with RISS/GNSS for reliable multi-sensor positioning in GNSS environments. Our work is also useful in environments where LiDAR and vision sensors can fail or in severe weather conditions such as snow and rain.

II. LITERATURE REVIEW

A. Automotive Radar Positioning Approaches

The usage of radars in positioning and navigation has been studied in different ways in the literature. Ashraf et. Al [25] used a single antenna Frequency Modulated Continuous Wave (FMCW) radar in acquiring a positioning solution. The methodology introduced was based on extracting the ground reflection and considering the resulting velocity as the vehicle's forward velocity. The presented system replaced the speedometer in updating the velocity components of the 3D-RISS mechanization. This work led to a position error of 7 meters in 50 seconds in artificially introduced GNSS outages. This work was then developed to estimate the vehicle's update from the confronting car in crowded areas [21][26]. This algorithm enhanced the RMSE error to 4 meters in 60 seconds.

The presented system's dependency on moving objects led to unprecedented errors in turns. The author then introduced a solution for the turning errors based on acquiring the azimuth from the magnetometer [27]. However, the magnetometer is very sensitive to electromagnetic wave interference.

Therefore, when the radar solution is mostly needed in downtown scenarios, the magnetometer may fail due to the crowd of the surrounding metallic objects [28]. To improve the results, the author proposed a multi-sensor fusion scheme that integrates 3D-RISS, a magnetometer, and a single antenna radar during GNSS outages [9]. A nonlinear system identification was utilized to further improve the multi-sensor positioning system, Fast-Orthogonal Search (FOS). The role of FOS is to generate a nonlinear error model for the Mag/Radar/RISS while the GNSS signals are available. Despite the improvement caused by FOS, it is a computationally expensive model, which prevents the possibility of real-time implementation. In addition, the work was based on simulated GNSS outages in ordinary scenarios where GNSS is available; therefore, the real behavior of the system was not examined properly.

Another research direction is based on electronic scanning radars in the literature. The research conducted using ESRs went through different stages. The detection of static objects is the base of the hierarchy. Dominik Kellner et al. [29] showed an intuitive static object detection technique using a single radar. Their proposed algorithm analyzes the received radial velocities and yaw rate of the objects. The largest group of similar linear movements are then considered stationary objects. The Random Sample Consensus (RANSAC) was then used to reject the outliers (moving objects). At the final stage, they could acquire the azimuth update due to mounting the radar on the left side of the vehicle. Yet, this mounting angle is neither realistic nor practical. The author integrated the same system into a multi-radar scheme [30]. That integration showed the ability to estimate the ego vehicle's yaw rate, and longitudinal and lateral velocities. Sarah H. Cen et al. [31] showed a static landmark extraction from FMCW radar. The usage of unary descriptors and compatibility scores allowed real-time data matching and mapping consecutively. Yet, the algorithm was based on a mechanically rotating radar on top of the vehicle; the high-definition mapping LiDAR system can easily outperform it.

Radar positioning can be realized by using one single radar, which is the most affordable and applicable to match the status quo, where most vehicles nowadays are equipped with one frontal radar. However, this research direction was either done on a single antenna radar, which does not give a full view of the frontal scene or using an array of the antenna without mounting the radar in front. There is another research direction that deals with radars as a visual-based system. They used the same feature extraction and scan-matching methods of the computer vision field [32-35]. Nevertheless, none of this research utilized a single radar to avoid several problems, such as the sparsity of data points, low signal-to-noise ratio, and poor feature distribution. These platforms were equipped with at least four radars, which is a futuristic approach that would not serve the current trend in the market. In this work, a radar-based positioning method is introduced. The method used is based on a single ESR frontal radar. Furthermore, the radar solution is fused with the 3D-RISS in GNSS outages to form a new integration called ESR/RISS/GNSS multi-system fusion.

III. METHODOLOGY

A. System Overview

The proposed system consists of three main stages. Firstly, it acquires the 3D-RISS positioning solution. Secondly, it detects the static objects in the ESR scan and acquires a radar positioning based on estimated velocity. Finally, it integrates both solutions using a loosely coupled EKF. The system overview is shown in Figure 1.
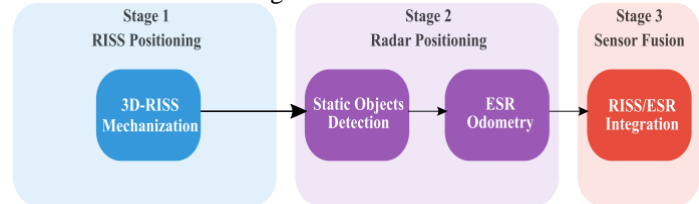

Fig. 1. System Overview

B. 3D-Reduced Inertial Sensors System

3D-RISS is an advanced inertial system that enhances positioning accuracy, decreases the associated drift, and reduces the computational complexity [36]. The enhancements achieved by the 3D-RISS are done by reducing the number of used inertial sensors. The reduction is based on strong constraints that fit any land vehicle. The inertial-based system has been discussed extensively in the literature [37-38].

C. Static Objects Detection

For land vehicles, tasks such as positioning, navigation, and path planning cannot be dependent on moving objects [39]. Therefore, the current vehicular technologies rely on other perception systems, such as LiDAR and Cameras, to identify the stationary objects in the surrounding environment, also known as landmarks. However, the proposed system presents a novel positioning system based on ESRs. Hence, it is essential to identify the static objects from the whole ESR scan to obtain a reliable radar-based positioning solution. Nevertheless, radar does not have the rich point-cloud associated with LiDAR or the numerous geometrical features that can be extracted from images. Thus, a detailed analysis of the ESR measurements is performed so that some distinguishing criteria can be concluded.

1) Detection Criteria

Building robust static object detection criteria requires a critical analysis of the ESR measurements. As clarified in Figure 2, the sensor receives the polar coordinates (range and angle) of the objects in the frontal FOV, and it also obtains the relative velocity between the objects and the ego-vehicle. Both range (distance) and angle are scalar quantities, which means only their magnitude information is obtained. Nevertheless, radial velocity is a vector quantity that has a magnitude and direction. The direction of velocity measurement has a significant impact, as it defines the movement behavior of the surrounding objects. More specifically, the relative velocity is not equivalent to the speed of the surrounding object; it is dependent on the relative motion between the ego-vehicle and the object. If the object is moving away from the ego-vehicle, the corresponding radial velocity will be positively signed. On

the contrary, if the object is getting closer to the ego-vehicle, its radial velocity will be negatively signed.

Indeed, a stationary object does not exert any force, and it remains still; it always has a zero-velocity magnitude. However, as the ego-vehicle is moving, metallic landmarks are detected as moving objects that have radial velocities. As the sensor is mounted on the center of the frontal bumper, any static object will have a negative-sign radial velocity; its direction is pointing towards the ego-vehicle. Nevertheless, the landmarks are most of the time located on both sides of the road. Hence, they are not having the same velocity as the vehicle's forward velocity. Their magnitudes are the resultant of the vehicle's lateral velocity and forward velocity; it means that the object's azimuth angle is correlated to both the range and the radial velocity.
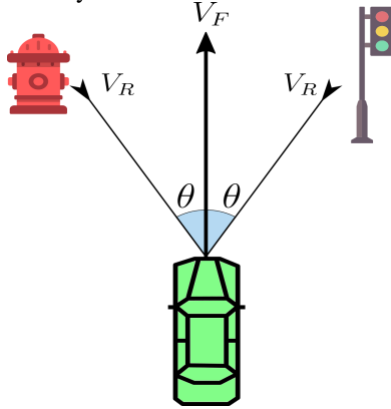

Fig. 2. ESR Scanned Objects Features

Static objects also have other observed properties that define them in the ESR scan. Since they do not exert force, they most likely exist in consecutive scans more frequently than moving objects. However, this relationship depends on the ego-vehicle speed too. The second observation is that in urban areas, indoor parking, and downtown, where ESR is needed the most, the landmarks represent the majority of the scene. Additionally, these areas are mostly congested so that the other vehicles can also act as static objects. This observation can also be interpreted as their radial velocities are very close to each other, and they form most of the feature set matrix.

Based on the previous observations, the following criteria were developed:

1) All static objects have negative radial velocity values.
2) The vehicle does not exert any lateral movement. Hence, lateral velocity magnitude is neglected.
3) The static objects are most of the scene in the areas of ESR positioning operation (downtown areas).
4) The most frequently consecutive detected object velocity in a scan will belong to the set of static detections.

2) Velocity Transformation

The radial velocities of static objects do not directly represent the vehicle's velocity. It is not conjugate to the vehicle's forward velocity due to the correlation between the angle of arrival and the detected relative velocity. The relative velocity of a static object is the result of the longitudinal (forward) velocity V_y and the lateral velocity V_x. The computation of relative velocity is shown in Equation 1.

$$V_R = V_y \cos\theta + V_x \sin\theta \qquad (1)$$

Where V_y is the forward velocity, V_x is the lateral velocity, and θ is the bearing angle between the object and the sensor.

A pre-processing step of the detector stage is to discriminate the velocity measurements of the stationary objects from the moving objects. For this purpose, a modification of the radial velocity computation is considered. This modification relies on the second criterion, where the vehicle's lateral velocity is minimal so that it can be neglected. This step simplifies the problem from finding a solution from two unknown variables (V_x, V_y) to depend on V_y only.

$$V_y = \frac{V_R}{\cos\theta} \qquad (2)$$

The impact of the transformation process is shown clearly in Figure 3, where the moving objects are considered outliers. A single ESR scan is shown in the figure, where 20 objects are detected, and their radial velocities are plotted. The original radial velocities are shown in the top figure, where it can be depicted that the graph does not have a distinct trend; the detectors might consider either a small number of static objects or include moving objects in the output. On the contrary, the bottom figure demonstrates the transformed velocities, where we can observe three distinct outliers, and the other velocities are ranging at 10 m/s with a margin of $\pm$ 0.1 m/s. The static object detectors should have accurate detection on the right graph. Moreover, the top figure includes all outliers to be detected, including the three clearly identified ones in the bottom figure. However, the purpose of the top figure is to demonstrate that before transformation, there are no distinct outliers due to the high variation in velocities. Furthermore, a percentage of static objects can be filtered along with moving objects.

3) Static Object Detectors

According to the previous discussion, the detectors are mainly outlier rejection methods. An outlier, as a term, refers to an abnormal value that deviates from the scattered population; in our case, it refers to a moving object that differs from most of the measurements. An outlier rejection method estimates the dispersion of the data points.

a) Median Absolute Deviation (MAD)

The Median Absolute Deviation (MAD) is a robust measure of the variability in the sample set. Unlike the standard error of the mean, the MAD relies on the median, from which it gets its robustness [40]. The breakdown point term gives a deep insight into the robustness of the MAD method. The breakdown point b_θ in statistics is the proportion of the outliers to the population, at which the statistics become vulnerable to outliers and not considered robust. By shedding light on the standard error of the mean, its breakdown point is $(b_{\bar{X}} = 0)$, which means that the mean $\bar{X}$ and the standard deviation $\bar{\sigma}$ are both vulnerable to outliers unless the size of the sample set is large enough. On the contrary, the MAD has a breakdown point $(b_{\tilde{x}} = 0.5)$; this is interpreted as if the

percentage of outliers in the sample set is lower than 50%, the MAD will be able to reject it robustly. In most cases, a sample set would not involve 50% of outliers; it is a rare condition. MAD is also considered a robust consistent estimator of the standard deviation σ, while the standard error is even non-robust in this estimation.
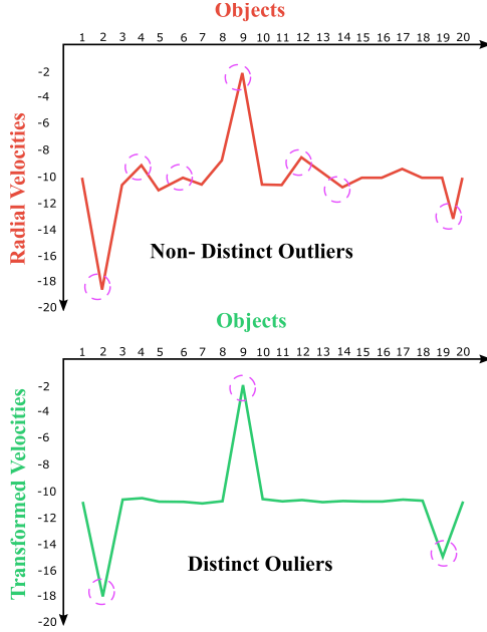

Fig. 3. Example of the Transformation effect on the outliers distinguishing process

MAD value is computed by getting the median of the absolute distances between the data points and the median sample, as shown in Equation 3:

$$MAD = median\left(\left|V_{y_i} - \widetilde{V_y}\right|\right) \qquad (3)$$

where MAD is the median absolute deviation measure, V_{y_i} is a transformed velocity of object i in the ESR scan set of objects, and $\widetilde{V_y}$ is the median of the set.

The MAD estimator of the standard deviation is given in Equations 4 and 5.

$$\hat{\sigma} = S \cdot MAD \qquad (4)$$

$$S = \frac{1}{\Phi^{-1}\left(\frac{3}{4}\right)} \cong \frac{1}{1.4826}\bigg|_{\mathcal{N}(\mu,\sigma)} \qquad (5)$$

Where $\hat{\sigma}$ is the standard deviation estimator, S is a scale factor, $\Phi^{-1}\left(\frac{3}{4}\right)$ is the quantile function, also known as the inverse of the cumulative distribution function, and $\mathcal{N}(\mu,\sigma)$ is the normal distribution.

For a normally distributed data the quantile function $\Phi^{-1}\left(\frac{3}{4}\right)$ is given to be 1.4826 approximately [41]. In relation to this derivation, the MAD covers a span of 50% from the left to the right of the median. This derived relation is valid for any type of distribution.

The outlier detection using MAD needs an additional step [42]. Similar to the standard error method, where a z-score is used to detect the outliers, the outlier rejection using MAD can be done utilizing a modified z-score. The modified z-score gives a score for each measurement, and this score is used to measure the outlier strength. In other words, it explains how a single score differs from the typical score. In terms of standard deviation, it approximates the distance from the median. The modified z-score inherits the robustness of the MAD; outliers do not highly influence it compared to the standard z-score.

The standard z-score is computed as the difference between the sample and the mean divided by the standard deviation. However, the modified z-score depends on the MAD. Thus, the standard deviation should be estimated using the MAD as in Equation 6. By substituting (3) in the denominator and having the difference between the samples and the median in the numerator, the modified z-score gets the following shape:

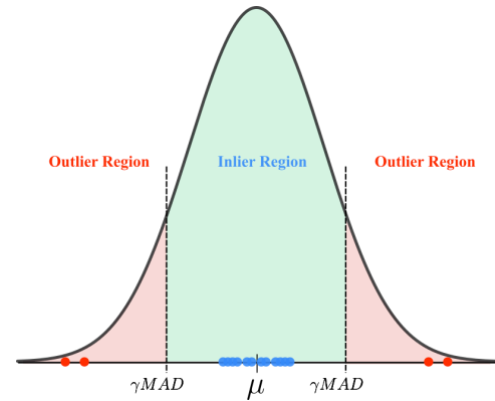$$Modified\ Z-Score = \frac{0.6745\left(V_{y_i} - \widetilde{V_y}\right)}{MAD} \qquad (6)$$

Fig. 4. MAD Based Outlier Rejection

The computation of the modified z-score is essential for the detection algorithm. That is because the filtration is done based on the scores of the objects. This filtration takes place using a threshold (γ), some may consider the threshold assigning is purely empirical. Even though there is no particular rule to choose γ, it has been shown that a threshold of 3.5 gives the most accurate outlier rejection. In a basic sense, any value higher than 3.5 would be considered an outlier. Any value higher than 3.5 will also be outside the 3-σ standard range. The visualization of the MAD detector operation is shown in Figure 4.

It can be determined that if the data are very close to each other, entailing high static to moving objects ratio, the MAD value would be small. And as the MAD is in the denominator of the modified z-score equation, this means that the smaller it is, the tighter threshold will be. Thus, very accurate data points will only be allowed.

Algorithm 1: MAD Based Static Objects Detector
1   **Input:** Transformed Velocities $V = \{v_1, v_2, \ldots\ldots, v_N\}$
2   **Output:** Static Objects $O = \{o_1, o_2, \ldots\ldots, o_N\}$
3   **Begin**
4   Initialize γ
5   MAD (V) = $Median \ |V - Median(V)|$
6   Modified Z-score (V) = $0.6745 \frac{|V - Median(V)|}{MAD\ (V)}$
7   **foreach** v_i in V **do**
8   **if** $score_i$ in Modified Z-score (V) **is less than** or **equal** γ **do**
9             $O = append\ (v_i)$
10   **end if**
11   **end**
12   **End**

Algorithm 1 shows the pseudo-code of the MAD-based detector. Firstly, it takes the transformed velocities set V in a single scan as an input. The second step is to initialize the threshold value (γ), so that the outliers are considered beyond the center of the distribution. The computation of the MAD value on the velocity set and the modified z-score vector is essential before the thresholding iteration. The filtration takes place in the iteration; as for the whole score vector, if the $score_i$ of object's velocity v_i is less than or equal to the threshold, it is stored. Finally, the objects that pass the threshold are appended in a list of static objects O.

b) Percentile-based Detector

The percentile detector is much simpler than the MAD, in terms of concepts. It divides the distribution into percentiles, where one is considered as an inlier region. The percentile detector is very similar to the Interquartile Range (IQR) Score, but it is not restricted to 25% percentiles of the data. Similar to IQR, the percentile-based outlier rejection does not assume a Gaussian distribution of the sample set. In the IQR outlier rejection method, The IQR value relies on the values of the first and third quartiles. The first quartile (Q1) is the median of the data points that underlies the lower half of the sample set, and it carries 25% of the numbers in the dataset below it. The third quartile (Q3) is the median of the upper half of the dataset and holds 25% of the numbers in the dataset above it. The IQR is computed by getting the difference between the first and third quartiles as in the following formula:

$$IQR = Q3 - Q1 \tag{7}$$

This technique for outlier rejection considers any value that lies above Q3 by 1.5×IQR or below Q1 by 1.5×IQR as an outlier and can then be removed from the dataset.

The percentile detector is based on similar principles. However, it is much simpler as it depends on a threshold γ in percentage so that the percentiles on the left and the right to it are considered outliers. The clarification of this technique is shown in Figure 5.
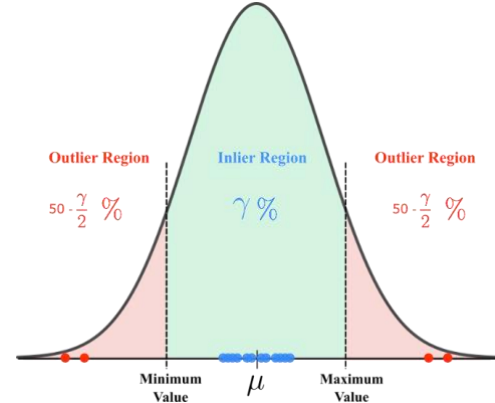

Fig. 5. Percentile Based Outlier Rejection

c) RANSAC-based Detector

RANSAC algorithm is a non-deterministic iterative method for estimating the parameters of a given model that contains a proportion of outliers [43]. RANSAC technique generates candidate solutions by using the minimum number of random samples of the observations. RANSAC technique is defined by two steps. In the first step, RANSAC randomly selects a subset of the data points; then, it tries to compute the parameter of both a fitting model and the corresponding model on this small subset. Secondly, RANSAC checks the entire sample set for data points that fit with the fitting model of the small subset. A data point is considered an outlier if it does not underlie a given error threshold. These two steps occur iteratively until the number of inlier samples matches a given threshold α.

RANSAC requires some assumptions to be fulfilled in order to succeed in rejecting the outliers [44]. It assumes that the outliers are few in the data and that there are enough inliers to fit a fitting model of a small subset. In the designed RANSAC detector, the input points were based on the correlation between the radial velocities and their corresponding azimuth angle. In other words, if a line is drawn to fit the static objects on a graph, they would have a unique trend that filters them out. Therefore, the inputs of the RANSAC detector are the radial velocities and the azimuth angles. However, RANSAC is dependent on some empirical parameters that control the algorithm's output [45]. These parameters are:

1) S: The smallest size of a sample set to be randomly chosen. The minimal number of samples is two, and there is no rule to select this value.
2) α: The error threshold within which the data points are considered inliers.
3) N: The maximum number of iterations at which the RANSAC algorithm terminates.
4) I: The ratio of detected inliers at which RANSAC terminates.

Once these parameters are assigned, the RANSAC becomes ready to iterate the two steps mentioned earlier. It firstly estimates a fitting line on a random small sample subset, then tries to fit the whole sample set to that line by measuring the Euclidean distances, the errors. Finally, the fitted points are stored in a list considered as static objects.

Based on the above elaboration of the three static object detectors, the MAD has the superiority. The main reason for this superiority is that it has proven statistical robustness by a breaking point of 0.5, which means it will reject any outlier in the data unless the outlier's percentage is 50%. Yet, both percentile detector and RANSAC have a totally empirical parameters adjustment, which would not be assured to achieve a certain level of robustness. However, as the dataset size increases, the RANSAC should perform better, whereas MAD will have the same robust performance on both small and big datasets.

D. Radar Odometry using Ego-velocity Estimation

The first step of the ESR odometry is averaging the transformed velocities of the static objects to obtain the forward velocity of the vehicle at the time epoch k.

$$V_F = \frac{1}{N_k} \sum_{i=1}^{N_k} V_{y_i}^k \qquad (8)$$

Where N_k is the number of Static Objects at time epoch k, $V_{y_i}^k$ is the transformed velocity on the forward axis of object i at time epoch k, and V_F is the obtained forward velocity from the ESR.

As shown in Figure 6, the extracted forward ESR velocity should be transformed to the local-level frame (LLF). This transformation is essential to compute the 2D-position components (latitude and longitude). The azimuth angle of the vehicle is the main factor in this computation, and it is always laid between the vehicle's forward axis and the north direction. As in Equation 9, the calculation of the azimuth angle is:

$$\dot{A} = -(\omega_z - \omega^{ie} \sin(\varphi)) \qquad (9)$$

Where $\dot{A}$ is the azimuth rate, ω_z is the heading gyroscope, ω^{ie} is the earth's rate of rotation, and φ is the latitude.
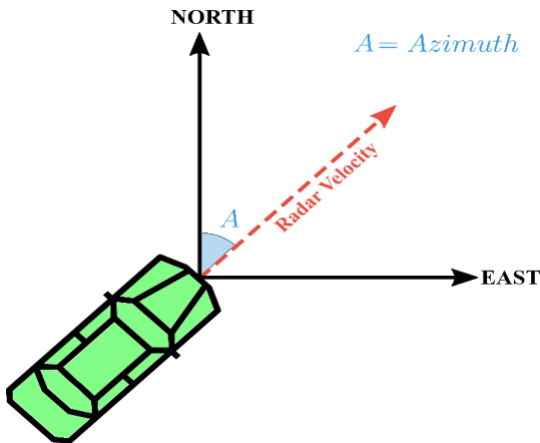

Fig. 6. ESR velocity transformation to the Local Level Frame (LLF)

In Equations 10 and 11, the transformation to the LLF takes place to compute the 2D-velocity vector. However, this projection utilizes only the azimuth angle and omits the pitch angle. This omission is valid due to the condition of land vehicles rarely exerting substantial movements around the y-axis.

$$V_{ESR_{East}} = V_F \, Sin \, A \qquad (10)$$
$$V_{ESR_{North}} = V_F \, Cos \, A \qquad (11)$$

Where $V_{ESR_{East}}$ is the vehicle's east velocity, $V_{ESR_{North}}$ is the vehicle's north velocity, and A is the azimuth angle.

With a known initial position, the current position can be obtained using:

$$\begin{bmatrix} \dot{\varphi}_{ESR} \\ \dot{\lambda}_{ESR} \end{bmatrix} = \begin{bmatrix} \dfrac{V_{ESR_{North}}}{(R_N + h)} \\ \dfrac{V_{ESR_{East}}}{(R_M + h)\cos(\varphi)} \end{bmatrix} \qquad (12)$$

Where $\dot{\varphi}_{ESR}$ is the latitude rate, $\dot{\lambda}_{ESR}$ is the longitude rate, and h is the altitude, which can be obtained from the 3D-RISS. The ESR positioning is used in the vehicle navigation by a loosely coupled EKF 3D-RISS/GNSS integration.

E. Multi-Sensor Fusion Model

The fusion of ESR, together with both GNSS and RISS, is performed using a de-centralized EKF scheme. In the traditional RISS/GNSS integration, the GNSS gives position and velocity updates, which reset the 3D-RISS position errors and estimates the gyroscope bias [46]. However, in challenging environments such as downtown areas, the GNSS solution suffers from errors like multipath or full signal blockage. A GNSS update in these scenarios will deviate the solution drastically, and instead of correcting the 3D-RISS errors, it will mislead the EKF to undesired instability. Hence, the ESR positioning update is utilized as an alternative update to the GNSS in such scenarios. Unlike GNSS, areas like urban canyons or indoor parking are full of metallic objects, which leads to better ESR positioning solutions. The block diagram of the proposed de-centralized loosely coupled integration is shown in Figure 7.
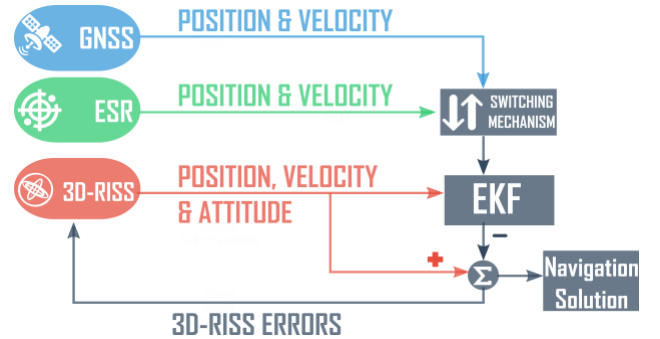

Fig. 7. ESR/RISS/GNSS de-centralized loosely coupled EKF Integration

Given that the integration scheme is loosely coupled and it is switching between GNSS and ESR with the RISS, the system's model is represented in the error state model, and the state vector is identical [46]. Equation 13 shows the system model.

$$\delta x_k = \Phi_{k-1} \, \delta x_{k-1} + G_k \, \omega_k \qquad (13)$$

where δx_k is the error state vector at epoch k, Φ_{k-1} is the state transition matrix for the previous epoch $k-1$, G_k is the noise distribution matrix, and ω_k is the process noise - White Gaussian Noise (WGN) with zero-mean & covariance Q_k.

The error state vector δx_k in Equation 14 contains nine states (3D-position, 3D-velocity, azimuth, acceleration bias drift, and gyro bias drift) to correct the 3D-RISS solution

when the GNSS updates are available. Equation 14 illustrates the error state vector.

$$\delta x_k = [\delta\varphi \quad \delta\lambda \quad \delta h \quad \delta v_e \quad \delta v_n \quad \delta v_u \quad \delta A \quad \delta a_{od} \quad \delta b_z]^T \tag{14}$$

where $\delta\varphi$, $\delta\lambda$, and δh are the position latitude, longitude, and altitude errors, respectively. δv_e, δv_n, δv_u are the east, north, and up velocity errors, respectively. δA is the azimuth error, δa_{od} is the stochastic odometer scale factor error, and δb_z is the gyroscope stochastic drift error.

The main difference in the ESR/RISS integration scheme is in the measurement updates, as different states are observed. The ESR updates the latitude, longitude, east and north velocity measurements. Thus, a new measurement design matrix H_{ESR} is required. The measurement model is shown in Equation 15.

$$\delta z_{ESR} = H_{ESR}\,\delta x_k + \varepsilon \tag{15}$$

Where δz_{ESR} is the measurement vector with size 4x1, H_{ESR} is the measurement design matrix with a size 4x9, and ε is the noise of the radar position measurement - WGN with zero-mean & covariance R_{ESR}.

The measurement vector entails the difference in measured latitude and longitude from the ESR and RISS. It is given in Equation 16.

$$\delta z_{ESR} = \begin{bmatrix} \varphi_{RISS} - \varphi_{ESR} \\ \lambda_{RISS} - \lambda_{ESR} \\ V_{RISS_{East}} - V_{ESR_{East}} \\ V_{RISS_{North}} - V_{ESR_{North}} \end{bmatrix} \tag{16}$$

The measurement design matrix is shown in Equation 17.

$$H_{ESR} = \begin{bmatrix} 1 & 0 & 0 & 0 & 0 & 0 & 0 & 0 & 0 \\ 0 & 1 & 0 & 0 & 0 & 0 & 0 & 0 & 0 \\ 0 & 0 & 0 & 1 & 0 & 0 & 0 & 0 & 0 \\ 0 & 0 & 0 & 0 & 1 & 0 & 0 & 0 & 0 \end{bmatrix} \tag{17}$$

Similar to GNSS in the measurement update, the measurement noise vector has a zero-mean Gaussian distribution with covariance matrix R_{ESR} that is calculated at each epoch. The R_{ESR} matrix carries the variances of the measured states in its diagonal. The R_{ESR} plays a significant role in the accuracy of the output solution. As a rule of thumb, as the ESR measurements are more abundant in features, the accuracy will be enhanced, and the noise will decrease. However, the initialization of the noise covariance matrix affects the solution convergence. It was observed during the experiments that an initialization using lower values leads to better results. The measurement noise covariance matrix is shown in Equation 18.

$$R_{ESR} = \begin{bmatrix} \sigma^2_{\varphi_{ESR}} & 0 & 0 & 0 \\ 0 & \sigma^2_{\lambda_{ESR}} & 0 & 0 \\ 0 & 0 & \sigma^2_{V_{ESR_{East}}} & 0 \\ 0 & 0 & 0 & \sigma^2_{V_{ESR_{North}}} \end{bmatrix} \tag{18}$$

F. Switching Mechanism

The ESR/RISS/GNSS system prioritizes the measurement update sensor based on criteria designed from the GNSS

observations. As a rule of thumb, when GNSS is available, it has the highest priority to dominate the positioning solution, as it is the most robust. It will also be used to update the RISS solution and reset the errors. Moreover, ESR and RISS are dead reckoning, so they need initial position values from GNSS. The GNSS has some indicators associated with its positioning solution that indicate its quality. These indicators are the geometry of satellites represented in the GDOP values, the standard deviation of the GNSS 3D-position update, and the number of satellites.

The GNSS needs at least four satellites to get a positioning solution. However, the accuracy of the solution increases with the increase of available satellites. The geometry of the constellation plays a significant role, as bad geometry leads to poor position accuracy. The GDOP indicates the geometry of the available satellites; it was observed that a GDOP value higher than two would lead to poor position performance for the GNSS solution. Finally, a higher standard deviation of the GNSS 3D position would also result in a GNSS positioning error. Therefore, a threshold of 3 meters was set to the GNSS standard deviation at which it switches. Algorithm 2 shows the switching fuzzy mechanism.

Algorithm 2: ESR/RISS/GNSS Switching Mechanism	
1	**Input:** Dilution of Precision Values, 3D-Position Standard Deviation, number of satellites
2	**Output:** Switch to the ESR positioning solution
3	**Begin**
4	**Acquire** GDOP
5	**if** GDOP **is more than** 3 **do**
6	**if** GNSS satellites **< 4 do**
7	**If** GNSS 3D-position standard deviation **is > 5 do**
8	$\dot\varphi_{GNSS}, \lambda_{GNSS} \to \dot\varphi_{ESR}, \lambda_{ESR}$
9	$\delta z_{GNSS} \to \delta z_{ESR}$
10	$H_{GNSS} \to H_{ESR}$
11	$R_{GNSS} \to R_{ESR}$
12	**end if**
13	**end if**
14	**end if**
15	**end**

IV. EXPERIMENTAL SETUP

The experimental framework carried out in this work is divided into the road trajectories and the experimental setup, which includes the onboard sensors and the vehicle utilized. In order to test the methods presented, a pair of challenging and long road trajectories were conducted in Toronto, Ontario, Canada, by a testing minivan. The sensors setup is divided into an exterior testbed mounted on the vehicle and an internal testbed mounted in the trunk. The external testbed consists of an ESR, as shown in Figure 8. The ESR used in this research is the DELPHI ESR 9.21.15. It has two modes of operation, long-range and mid-range. The long-range has a FOV of ±10 degrees and a range of 175 meters, while the mid-range features a ±45 degrees FOV and a range of 60 meters. It can measure velocities from -100 m/s to +24 m/s and detects up to

64 objects in both simultaneously operating modes. The Delphi ESR 9.21.15 has an update rate of 20 Hz, and operates at a frequency of 77 GHz and takes a 24 V DC. The ESR is mounted precisely on the center of the vehicle's front bumper; this setup is typical to the industrial scheme, which uses this mounting in the ADAS functionalities.

The interior testbed is mounted in the back of the minivan, in the trunk. A customized mounting was designed to stabilize the sensors and to maintain them centralized. As shown in Figure 9, three major units form the interior testbed: a reference GNSS NovAtel-SPAN ProPak6, a tactical grade KVH 1750 IMU, and a low-cost MEMS-grade VTI-IMU. The ProPak6 and KVH units were used to generate the reference solution utilizing the NovAtel span unit, the VTI-IMU was used in the RISS mechanization, and the DELPHI ESR 9.21.15 was used in the ESR/RISS/GNSS integration. The sensors were synchronized at an update rate of 5 Hz. The data is analyzed on an x64-based processor, Intel Core i7-8750H CPU, at 2.20 GHz, with a 16 GB RAM running Windows 10 with an NVIDIA GeForce GT 1050 Ti GPU. The map overlays were created using MATLAB and Google's cloud platform utilizing an API key to download the maps directly in the output plot.

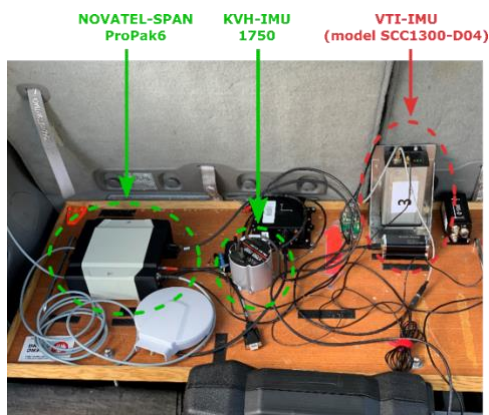Fig. 8. Exterior testbed shows the mounted Delphi ESR 9.21.15.

Fig. 9. Interior testbed installed inside the minivan's trunk showing the measurement units.

V. RESULTS

A. Velocity Estimation using Static Objects Detectors

Three static object detectors were introduced, which are MAD-based, Percentile-based, and RANSAC-based detectors. In the experimental phase, the three methods were examined to identify which is best for the velocity estimation to contribute to the positioning solution. As mentioned earlier, each algorithm has its set of hyperparameters, and their values are presented in Table 1.

TABLE I
STATIC DETECTORS HYPERPARAMETERS

Method	Hyperparameters	Values
MAD	γ_{MAD}	3.5
Percentile	$\gamma_{Percentile}$	70%
RANSAC	S	2
	N	100
	α	0.1
	I	4

The threshold γ_{MAD} was chosen 3.5 to approximately include the 3-sigma rule of a normal distribution, which corresponds to 99% of the distribution. Similarly, the percentile inliers percentage used was 70% to cover most of the sample set. However, the RANSAC hyperparameters are empirical, and the choice of values is based on trial and error. Therefore, the RANSAC hyperparameters values were set to be very small to adapt to the sparsity of the data. The typical ESR scan-set in Toronto trajectories had a size that varied between 20 objects to 50 objects. It was rarely observed that some of the sample sets reached the maximum objects detections of 64 objects.

The data sparsity is a significant burden for any outlier rejection method. As the number of samples increases, the accuracy of the rejection methods increases. Although the MAD outlier rejection technique follows the same rule, it is still very robust with sparse data and more favorable than the others; that is because of its breakpoint of 0.5. In contrast, the RANSAC method performs well in large datasets and poorly with small data sizes. The percentile method is located in the middle between the two other techniques, where it is susceptible to the used hyperparameter. Percentile-based outlier rejection works with all types of distribution, so if the data is normally distributed, a 99.73% hyperparameter will represent a 3-sigma.

Figure 10 shows a case study from the estimated velocity errors of trajectory one that is shown in Figure 11; it confirms the mentioned analytical view of the statistical methods with the sparse ESR scan-sets. The MAD-based detector was able to identify the most accurate static objects for almost one minute, keeping error boundaries of ± 0.5 m/s. The 70% threshold of the percentile-based method covered some moving objects in the FOV, which resulted in a higher error than the MAD with a boundary of 3 m/s and less error than the RANSAC. Undoubtedly, the RANSAC had a dramatic failure with very high periodic residual errors. The RANSAC is a random sampling method, which allows it to detect inliers in massive datasets where the outliers are highly variant than the inliers. Additionally, RANSAC depends on the correct assumption of the mathematical model of the data; in other words, the relation between the data points should be accurately observed. All these factors contradict with the sample sets available in each ESR scan, where the data is too sparse, and the relation between the radial velocities and their

corresponding angles is not apparent. Nevertheless, RANSAC is a favorite candidate with a higher multi-ESR system, where the number of points is much higher than 64 objects in the space.
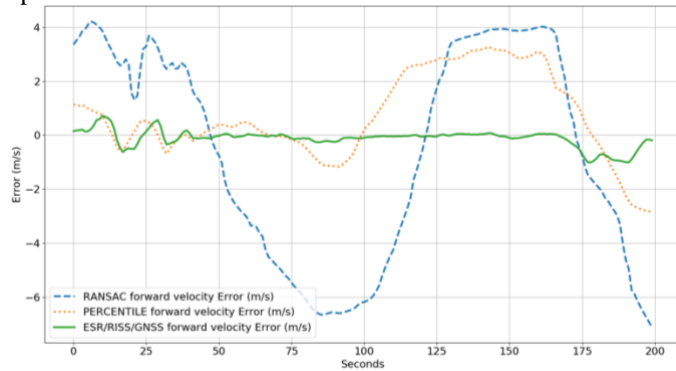

Fig. 10. Case Study on the errors of the Velocity Estimation using static detectors. The dashed green line refers to the MAD, the yellow to the Percentile, and the blue to the RANSAC.

B. Road Trajectory One

The first trajectory in the experimental phase was conducted in Toronto, Ontario, Canada. The vehicle's path was pre-designed to go through challenging GNSS areas, such as suburban and downtown areas. Additionally, the trajectory spans different driving scenarios, such as sharp and smooth turns, different angles, straight movement, and different traffic conditions. This trajectory surpassed 17 km and lasted for 60 minutes. Due to the existence of high-rise buildings that block the GNSS signals along the trajectory, four natural GNSS outages were observed during the path. Each GNSS outage has its own property, such as extended duration and distance, existence among high-rise buildings, and initialization from critical GNSS coverage areas. At each GNSS outage, the GNSS solution was totally unreliable; therefore, the proposed radar-based system aided the RISS mechanization. The resultant output is then compared to both the reference and the RISS-only solution.
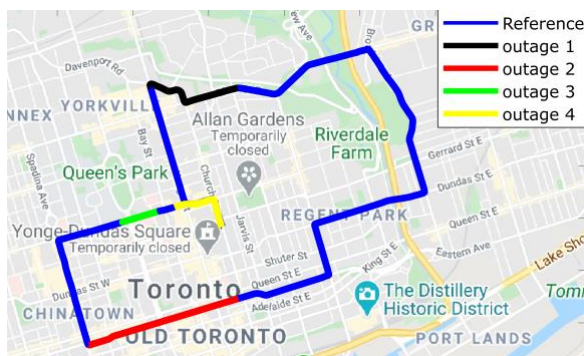

Fig. 11. Road trajectory one conducted in downtown Toronto, October 2019

1) GNSS Outage one: Multiple Turns Property

The first GNSS outage in the trajectory occurred beside the Toronto public library, as shown in Figure 12; in this place, the street is surrounded by high-rise buildings from one side, while the other sides are filled with typical buildings. Throughout this GNSS outage, the vehicle was exposed to several dynamics. For 5 minutes, along 802 meters, the

vehicle made four turns; two were smooth, and the others were sharp. The first turn took place exactly at the start of the GNSS outage, while the other three turns were consecutive and close to each other.
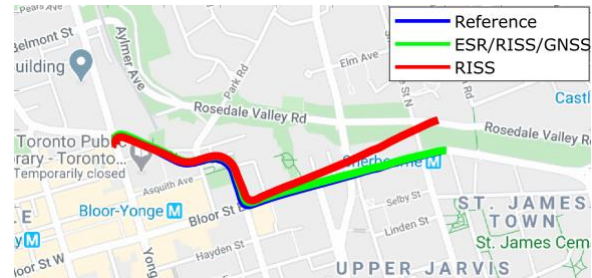

Fig. 12. GNSS outage one with multiple turns.

As the RISS mechanization always starts with a small drift for the short-term, it was almost conjugated to the reference in the first turn. However, the ESR/RISS/GNSS integration suffered at the beginning, as the method was initialized at a turn. If the static object detector is initialized at a turn, the odds of the static object's uncertainty become higher; consequently, the velocity estimation would be slightly misled. Afterward, the static object detection became more accurate, and the proposed ESR/RISS solution got close to the reference. At the same time, the RISS output drifted gradually with each turn due to the residual gyroscope errors that were not corrected in the absence of ESR updates.

The ESR/RISS solution excelled in this scenario, while the RISS output had a significant deviation from the reference. In terms of 2D position errors, the RISS solution has an RMS error of 32.6 m, while the proposed system enhanced the positioning by 65% and achieved an RMS error of 11.55 m. Consequently, the ESR-based system had a lower error percentage of the traveled distance, 1.44% of 802 m, while the RISS solution deviated about 4.1% of the same distance. The maximum error of the ESR/RISS/GNSS solution was about 19.2 m, but the RISS algorithm reached a boundary of 77 m.

2) GNSS Outage Two and Three: Straight Driving in Toronto Downtown Area

The second and third GNSS outages share one property, which is in driving behavior. Both took place while the car was moving in a straight line. However, the third GNSS outage shown in Figure 13 was shorter and occurred in a place with a lower count of high-rise buildings. Hence, the third GNSS outage had better initialization, as it started from a slightly open sky area beside Queen's Park, giving the opportunity for the GNSS solution to reset the RISS position errors and the gyroscope biases. The GNSS outage lasted for 3 minutes only and had the shortest distance in trajectory one outage of 365 m.

With fewer high-rise buildings, both RISS and ESR/RISS/GNSS systems had better positioning solutions in this area. Unlike GNSS outage one, the outage started before an intersection, at which the surrounding environment is rich in static objects such as traffic lights and signs. As a result, the velocity estimation was accurate enough to result in an accurate ESR/RISS solution following the reference solution. The proposed solution maintained the same behavior with

This article has been accepted for publication in IEEE Transactions on Vehicular Technology. This is the author's version which has not been fully edited and content may change prior to final publication. Citation information: DOI 10.1109/TVT.2023.3316612

11

> REPLACE THIS LINE WITH YOUR MANUSCRIPT ID NUMBER (DOUBLE-CLICK HERE TO EDIT) <

minimal drift since the straight-line movements have several static objects on both sides of the street in the frontal FOV of the car, unlike in turns. Similar to the first GNSS outage, the RISS algorithm had a similar behavior of gradual drift over time. However, this drift was not severe as there were not any turns either smooth or sharp; thus the impact of the gyro scale factor errors remains minimal.
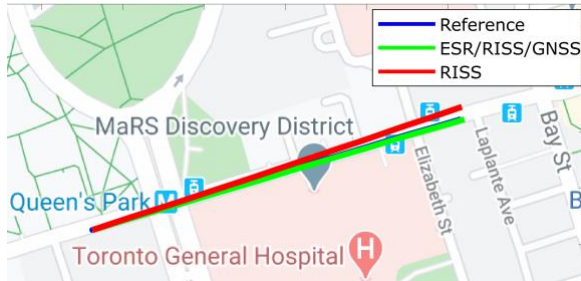

Fig. 13. GNSS Outage Three, straight driving in the downtown area.

As expected in short distance and time GNSS outages, both systems were very close to the reference. The RISS solution had an RMS error of 9.64 m, which is equivalent to 2.65% of the 365 m distance traveled, while the proposed system enhanced the error by 70%, achieving 2.9 m and 0.8% of the traveled distance.

Similarly, the RISS system had a maximum error of 12 m, while the ESR/RISS/GNSS algorithm enhanced that error by 50% to achieve 6.1 m.

On the contrary, the second GNSS outage shared the straight driving behavior but was exposed to worse conditions, such as poor initialization and moving in the downtown region. The GNSS outage started in the Old Toronto district and lasted 7 minutes and a total traveled distance of 538 m. It took place in a street between several skyscrapers, which means the initialization of the RISS and the proposed system is imperfect.

An improper initialization can lead to a faster drift and higher overall error in dead reckoning solutions. However, as was expected from the ESR, the downtown area is rich in stationary objects, so it had better velocity estimation and, consequently, better positioning solution in comparison to the RISS.
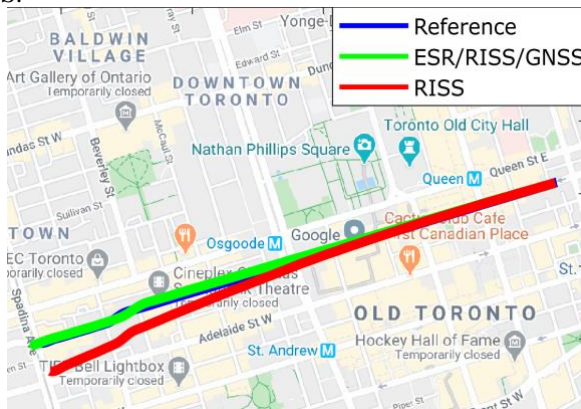

Fig. 14. GNSS Outage Two, Downtown area with High Rise Building

The illustration in Figure 14 shows a slight deviation in both systems. Nevertheless, the numbers do not exactly match the observation in the figure. Surprisingly, the RMS error of

the RISS mechanization is about 34.4 m, with 6.4% of the 538 m traveled distance. Like the previous GNSS outages, the ESR-based solution enhanced the positioning by 30%, with an RMS error of 24 m, which is equivalent to 4.5% of the GNSS outage distance. In terms of maximum error, the numbers are much higher, as the RISS had a maximum deviation of 92.4 m, and the proposed system enhanced it by 35%, which is equivalent to 60.3 m. These errors are mostly in the longitudinal direction and cannot be depicted in the results displayed on the map. Such errors could be caused by scaling or shifting in measurements due to unprecedented biases.

3) GNSS Outage Four: Sharp Turn in a Downtown District

The fourth and last GNSS outage of trajectory one occurred in the same region where the trajectory started. This outage has a duration of 4 minutes and a traveled distance of 502 m, which is considered moderate in terms of time and distance. However, it shares the same challenging property as GNSS outage two; it started in the downtown district, where several skyscrapers surrounded the vehicle. Nevertheless, the initialization of the algorithm was better than GNSS outage two, resulting in better overall positioning performance.

As shown in Figure 15, The fourth GNSS outage started from a straight driving condition and experienced a slight angular movement before a very sharp turn in the middle. The straight driving initialization in the downtown area offered the static object detectors massive features, which in turn decreased the error at the beginning and impacted the consistency of the ESR-based positioning with very low position drift. Similarly, the better initialization allowed the RISS to maintain adequate performance for a longer time before drifting, limiting the position error growth of the RISS solution.
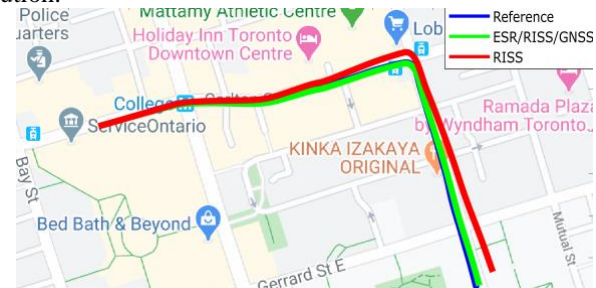
Fig. 15. GNSS Outage Four, Sharp Turn in Toronto Downtown

This GNSS outage has the second-lowest position errors in trajectory one after outage three. The ESR/RISS/GNSS system had a 4 m RMS error, which is equal to 0.8% of the 502 m traveled distance. The proposed system enhanced the RISS solution by 74%, where the RISS algorithm had an RMS error of 11.17 m and 2.22% of the traveled distance. In similar behavior, the ESR-based solution had a better maximum error of 8.5 m, while the RISS method deviated to 30.4 m; the overall enhancement is equivalent to 80%.

C. Road Trajectory Two

The second trajectory, shown in Figure 16, was conducted on the 13th of October in Toronto, two hours later than the first trajectory. It covered a distance of 28.7 km and lasted for a

total of 75 mins. In contradiction to the first trajectory, the number of GNSS outages is less, and it didn't span several challenging environments as the first one. Nevertheless, there were two outages: one of them was an indoor parking. In closed areas such as tunnels, buildings, and indoor parking, the GNSS signals are entirely blocked, and the usage of other systems is essential.

Fig. 16. Toronto Trajectory Two with GNSS Outages

1) GNSS Outage Five: Suburban Area

The fifth outage took place in the second trajectory; it occurred in a suburban district, where GNSS signals are less noisy than the previously mentioned conditions. However, testing the proposed solution in such conditions is essential to emphasize that it works in most driving scenarios. This GNSS outage is quite extended in terms of traveled distance, as it surpassed 860 m. However, it has a moderate duration of 5 minutes. As shown in Figure 17, it consists of two sharp turns and dual extended straight movements. The GNSS outage started beside Dufferin Grove Park with proper initialization. The figure shows that the ESR-based system did not deviate in most of the GNSS outages. The behavior of the proposed system shows the richness of static features in such scenarios. Nevertheless, the first turn affected the RISS behavior, which deviated within the extended straight movement.
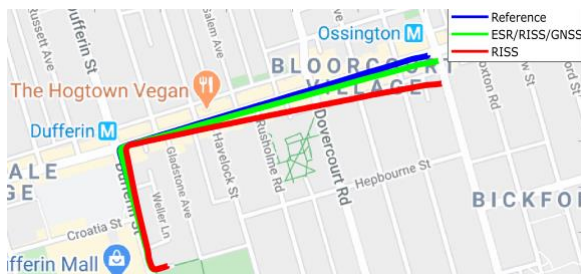

Fig. 17. GNSS Outage five, suburban area

Both systems deviated with different growth rates, as the ESR-based system sustained under 5 m error for almost 3.3 minutes, then it exceeded 10 m after the fourth minute. On the contrary, the RISS took almost half the duration to reach 5 m errors and faster to surpass 10 m. In terms of RMS errors, the RISS solution resulted in 30.4 m, that is 3.5% of the 860.2 m distance traveled. The proposed ESR/RISS system enhanced this performance by 70% and reached 9.42 m, which is equivalent to 1.9% of the traveled distance. The RISS

mechanization had a maximum error of 75.8 m, while the ESR/RISS integration decreased the error measure by 62%, which is equal to 29.1 m.

Table 2 summarizes the five GNSS outages discussed in the results section.

TABLE II
2D RMS HORIZONTAL POSITION ERROR IN METERS DURING GNSS OUTAGES

Outage Number	Trajectory Number	Outage Duration	Distance Traveled	RISS RMS Error	ESR/RISS/GNSS RMS Error
1		5	801.56	326	11.6
2		7	538	34.5	24.2
3	Trajectory One	3	364	9.7	2.9
4		4	502.4	11.2	4
5	Trajectory Two	5	860.23	30.4	9.42
Average		4.25	540.5	20.6	9.5
Overall RMS Error Enhancement Percentage					54%

D. GNSS-Denied Outage: Multi-Level Indoor Parking

The sixth and final GNSS outage took place in a fully denied GNSS environment. The environment consisted of multi-level indoor parking in Toronto, as shown in Figure 18. In this GNSS outage, the presented switching algorithm was tested.

The switching algorithm is a priority-based framework; it consists of the GNSS quality indicators, which are the number of satellites, standard deviation, and DOP values. These features allowed us to achieve an accurate positioning for almost 11 minutes. As shown in the figure, before the indoor parking entrance, the vehicle was in an open sky area, which allowed the GNSS to reset the RISS errors. Afterward, the GNSS signal was blocked, and the switching mechanism controlled which system to rely on.
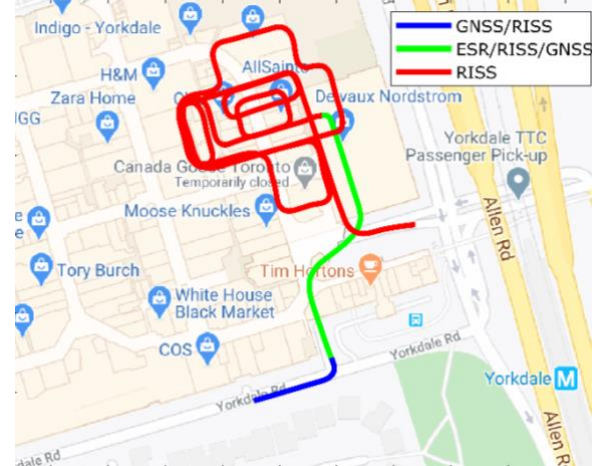
Fig. 18. Extended Indoor Parking GNSS Outage. A fully denied environment where GNSS signals are totally unavailable.

This indoor scenario showed the reliability of the switching mechanism and its significance in achieving better positioning solutions in all scenarios. The switching criteria can be adjusted and designed based on the used sensor. The RISS error was measured at the exit of the indoor parking when GNSS was available again. The error was about 6.5 m after 11 minutes. This error shows the significance of a perfect initialization, which could lead to minimal errors over extended GNSS outages.

VI. Discussion

The proposed methodology had reliable positioning results with an error percentage between 0.5 to 4% of the traveled distance in the GNSS outages. Additionally, it lowered the standalone RISS errors by percentages higher than 50% on all occasions. However, the standalone RISS showed a better performance in an indoor parking GNSS full denial that lasted for 11 minutes. These presented results led to various observations that define the behavior of the system in different stages.

Firstly, a single ESR suffers from a lack of features. Even though one radar is efficient for the tasks of land vehicles, the maximum of 64 objects (not mostly achieved) is very sparse for positioning purposes. Consequently, the static object detection-based velocity estimation is the most practical approach to rely on a single ESR. Secondly, the specified static object detection criteria are effective, and they define the characteristics of a static object. This was proved by the small error achieved by the MAD-based algorithm. Additionally, RANSAC is very sensitive to small data sizes, the mathematical relation between the points, and the hyperparameters. The failure of this detector occurred mainly due to the sparsity of data. However, in rich object environments, it might lead to better results but not as robust as the MAD. Thirdly, the behavior of the proposed ESR/RISS system and the standalone RISS algorithm are both shaped by the initialization step. A better initialization would lead to a more accurate positioning solution. The ESR system has superior accuracy over RISS in downtown areas, as they are crowded with static objects such as landmarks, signs, and traffic lights. Additionally, it performs better in a straight line, where the distribution of landmarks defines the road course and is almost equivalent on both sides. Finally, the RISS system excels when the R-covariance matrix is well-tuned, the initialization is accurate, and the driving dynamics are moderate with low speed and fewer turns.

Regarding the comparison with other perception sensors, challenging urban environments were utilized to collect and process similar trajectories using GNSS/RISS/LiDAR, as documented in [7]. The results indicate that LiDAR still offers a substantial enhancement in terms of positioning accuracy when compared to standalone 3D-RISS. For example, during a 10-minute outage, the standalone 3D-RISS exhibited an RMS error of 46.37 m, whereas GNSS/RISS/LiDAR demonstrated a significant improvement to 16.28 m, corresponding to a 64% reduction in the RMS error value. Additionally, the total distance traveled was 2 km, with the GNSS/RISS/LiDAR deviation of 2% compared to the RISS, which displayed a 6% deviation over the traveled distance. However, it is important to note that this improvement comes at the expense of increased computational complexity associated with LiDAR odometry. This includes various processes such as ego points removal, segmentation of ground points from the point cloud, point cloud clustering, denoising, down-sampling, and scan matching.

In terms of comparing with VO, a similar trajectory was conducted in an indoor GNSS-denied environment, as described in [47-48]. The trajectory took place in the parking garage of Yorkdale Shopping Center in Toronto, utilizing the same testing minivan employed in this study. The duration of the trajectory was 90 seconds, and the performance of three systems - 3D-RISS, VO, and RISS/VO - was evaluated. At the end of the 90-second trajectory, the RMS error of the VO system was approximately 14 m, while the standalone 3D-RISS solution achieved an RMS error of 9 m. However, the RISS/VO combined system demonstrated a further improvement, with an RMS error of around 3 m. It is worth noting that achieving this enhancement in performance requires sophisticated real-time computations. Furthermore, it is important to consider the impact of lighting conditions, such as shadowing, on the performance of VO. The VO system's performance is significantly affected by variations in light conditions, leading to potential degradation in accuracy. This highlights a limitation of VO systems, particularly in scenarios where lighting conditions are challenging. In summary, while VO provides a viable solution for indoor GNSS-denied environments, the integration of RISS with VO offers further improvement in accuracy. However, it is crucial to consider the computational complexity associated with real-time computations and the limitations of VO systems under certain lighting conditions, such as shadowing.

In conclusion, each perception sensor has its own advantages and limitations. Radar, for example, is an all-weather sensor capable of operating in diverse weather conditions. On the other hand, LiDAR and cameras impose a higher computational load, and their accuracy is susceptible to adverse weather conditions like rain or snow.
As a future direction for the research presented in this paper, a promising approach would be to employ smart sensor fusion techniques that combine the strengths of all available sensors while mitigating the limitations associated with each sensor. By leveraging sensor fusion, it becomes possible to harness the advantages offered by different sensors and overcome their individual constraints.

VII. Conclusion

The work proposed in this paper aims to enhance the positioning solution of land vehicles in different driving scenarios. The challenges associated with GNSS limit the ability to rely on them for positioning services for all environments. The dependence on standalone inertial navigation (INS or RISS) can help only over short GNSS outages. The proposed system is a radar-based multi-sensor fusion scheme, which utilizes a single ESR, inertial sensors, a vehicle's odometer, and GNSS to acquire the vehicle's position. It consists of various stages, where the positioning solution is the last one. The base stage in this research is static object detectors based on unique static object detection criteria and statistical outlier rejection method based on the MAD algorithm, which outperformed both the Percentile and RANSAC. The second stage was developing an ESR-based positioning solution fused with the RISS in the final stage utilizing an EKF integration scheme. This integration enabled resetting both the RISS position and azimuth errors during GNSS outages, thus providing continuous and reliable

positioning solutions better than standalone RISS in challenging and denied GNSS environments. Finally, a new switching mechanism between GNSS, ESR, and RISS in delivering the final positioning solution was introduced and discussed in this research.

REFERENCES

[1] C. Urmson *et al.*, "Self-driving cars and the urban challenge," *IEEE Intell. Syst.*, vol. 23, no. 2, pp. 66–68, 2008.

[2] W. Balid, H. Tafish, and H. H. Refai, "Intelligent vehicle counting and classification sensor for real-time traffic surveillance," *IEEE Trans. Intell. Transp. Syst.*, vol. 19, no. 6, pp. 1784–1794, 2017.

[3] C. Badue *et al.*, "Self-driving cars: A survey," *arXiv Prepr. arXiv1901.04407*, 2019.

[4] J. Georgy, A. Noureldin, and C. Goodall, "Vehicle navigator using a mixture particle filter for inertial sensors/odometer/map data/GPS integration," *IEEE Trans. Consum. Electron.*, vol. 58, no. 2, pp. 544–552, 2012.

[5] U. Iqbal, T. B. Karamat, A. F. Okou, and A. Noureldin, "Experimental results on an integrated GPS and multisensor system for land vehicle positioning," *Int. J. Navig. Obs.*, vol. 2009, 2009.

[6] M. M. Atia, J. Georgy, M. J. Korenberg, and A. Noureldin, "Real-time implementation of mixture particle filter for 3D RISS/GPS integrated navigation solution," *Electron. Lett.*, vol. 46, no. 15, pp. 1083–1084, 2010.

[7] A. Aboutaleb, A. S. El-Wakeel, H. Elghamrawy, and A. Noureldin, "LiDAR/RISS/GNSS Dynamic Integration for Land Vehicle Robust Positioning in Challenging GNSS Environments," *Remote Sens.*, vol. 12, no. 14, p. 2323, 2020.

[8] T. B. Karamat, R. G. Lins, S. N. Givigi, and A. Noureldin, "Novel EKF-based vision/inertial system integration for improved navigation," *IEEE Trans. Instrum. Meas.*, vol. 67, no. 1, pp. 116–125, 2017.

[9] A. Abosekeen, U. Iqbal, A. Noureldin, and M. J. Korenberg, "A Novel Multi-Level Integrated Navigation System for Challenging GNSS Environments," *IEEE Trans. Intell. Transp. Syst.*, 2020, doi: 10.1109/tits.2020.2980307.

[10] I. Skog and P. Handel, "In-car positioning and navigation technologies—A survey," *IEEE Trans. Intell. Transp. Syst.*, vol. 10, no. 1, pp. 4–21, 2009.

[11] A. R. Vetrella, G. Fasano, and D. Accardo, "Cooperative navigation in GPS-challenging environments exploiting position broadcast and vision-based tracking," in *2016 International Conference on Unmanned Aircraft Systems (ICUAS)*, 2016, pp. 447–456.

[12] A. Fernández *et al.*, "GNSS/INS/LiDAR integration in urban environment: Algorithm description and results from ATENEA test campaign," in *2012 6th ESA Workshop on Satellite Navigation Technologies (Navitec 2012) & European Workshop on GNSS Signals and Signal Processing*, 2012, pp. 1–8.

[13] D. Bolkas, "On the Estimation of Uncertainties and Fusion of Multi-Platform Geodetic Data," Queen's University, 2015.

[14] H. Y. Lim, *Autonomous vehicles and the law: technology, algorithms and ethics*. Edward Elgar Publishing, 2018.

[15] Z. Yang and S. Shen, "Monocular visual--inertial state estimation with online initialization and camera--IMU extrinsic calibration," *IEEE Trans. Autom. Sci. Eng.*, vol. 14, no. 1, pp. 39–51, 2016.

[16] Y. Sun, M. T. Rahman, T. B. Karamat, A. Noureldin, and Y. Gao, "Integrating Vision Based Navigation with INS and GPS for Land Vehicle Navigation in Challenging GNSS Environments," in *Proceedings of the 29th International Technical Meeting of The Satellite Division of the Institute of Navigation, Portland, OR, USA*, 2016, pp. 12–16.

[17] H. Ragab, S. Givigi, and A. Noureldin, "Leveraging vision-based structure-from-motion for robust integrated land vehicle positioning systems in challenging GNSS environments," in *Proc. 31st Int. Tech. Meeting Satell. Div. Institute Navig.(ION GNSS+)*, 2018, pp. 3098–3110.

[18] "Tesla Achieved The Accuracy Of Lidar With Its Advanced Computer Vision Tech." https://cleantechnica.com/2020/04/24/tesla-achieved-the-accuracy-of-lidar-with-its-advanced-computer-vision-tech/.

[19] E. Ward and J. Folkesson, "Vehicle localization with low cost radar sensors," in *2016 IEEE Intelligent Vehicles Symposium (IV)*, 2016, pp. 864–870.

[20] F. de Ponte Müller, "Survey on ranging sensors and cooperative techniques for relative positioning of vehicles," *Sensors*, vol. 17, no. 2, p. 271, 2017.

[21] A. Abosekeen, T. B. Karamat, A. Noureldin, and M. J. Korenberg, "Adaptive cruise control radar-based positioning in GNSS challenging environment," *IET Radar, Sonar Navig.*, vol. 13, no. 10, pp. 1666–1677, 2019.

[22] D. A. Robertson, D. G. MacFarlane, P. A. S. Cruickshank, D. R. Bolton, R. I. Hunter, and G. M. Smith, "High performance MM-wave radar techniques," 2006, doi: 10.1049/ic:20060104.

[23] M. Hoedemaeker, *Driving behavior with ACC and the acceptance by individual drivers*. IEEE, 2000.

[24] A. Moreira, P. Prats-Iraola, M. Younis, G. Krieger, I. Hajnsek, and K. P. Papathanassiou, "A tutorial on synthetic aperture radar," *IEEE Geosci. Remote Sens. Mag.*, 2013, doi: 10.1109/MGRS.2013.2248301.

[25] A. Abosekeen, A. Noureldin, and M. J. Korenberg, "Utilizing the ACC-FMCW radar for land vehicles navigation," in *2018 IEEE/ION Position, Location and Navigation Symposium (PLANS)*, 2018, pp. 124–132.

[26] M. A. Rashed, A. Abosekeen, H. Ragab, A. Noureldin, and M. J. Korenberg, "Leveraging FMCW-radar for autonomous positioning systems: Methodology and application in downtown Toronto," in *Proceedings of the 32nd International Technical Meeting of the Satellite Division of The Institute of Navigation (ION GNSS+ 2019)*, 2019, pp. 2659–2669.

[27] A. Abosekeen, A. Noureldin, and M. J. Korenberg, "Improving the RISS/GNSS land-vehicles integrated navigation system using magnetic azimuth updates," *IEEE Trans. Intell. Transp. Syst.*, 2019.

[28] M. Kok and T. B. Schon, "Magnetometer calibration using inertial sensors," *IEEE Sens. J.*, 2016, doi: 10.1109/JSEN.2016.2569160.

[29] D. Kellner, M. Barjenbruch, J. Klappstein, J. Dickmann, and K. Dietmayer, "Instantaneous ego-motion estimation using Doppler radar," 2013, doi: 10.1109/ITSC.2013.6728341.

[30] D. Kellner, M. Barjenbruch, J. Klappstein, J. Dickmann, and K. Dietmayer, "Instantaneous ego-motion estimation using multiple Doppler radars," 2014, doi: 10.1109/ICRA.2014.6907064.

[31] S. H. Cen and P. Newman, "Precise Ego-Motion Estimation with Millimeter-Wave Radar under Diverse and Challenging Conditions," 2018, doi: 10.1109/ICRA.2018.8460687.

[32] T. Giese, J. Klappstein, J. Dickmann, and C. Wöhler, "Road course estimation using deep learning on radar data," in *2017 18th International Radar Symposium (IRS)*, 2017, pp. 1–7.

[33] F. Schuster, C. G. Keller, M. Rapp, M. Haueis, and C. Curio, "Landmark based radar slam using graph optimization," in *2016 IEEE 19th International Conference on Intelligent Transportation Systems (ITSC)*, 2016, pp. 2559–2564.

[34] F. Schuster, M. Wörner, C. G. Keller, M. Haueis, and C. Curio, "Robust localization based on radar signal clustering," in *2016 IEEE Intelligent Vehicles Symposium (IV)*, 2016, pp. 839–844.

[35] S. H. Cen and P. Newman, "Radar-only ego-motion estimation in difficult settings via graph matching," 2019, doi: 10.1109/ICRA.2019.8793990.

[36] U. Iqbal, A. F. Okou, and A. Noureldin, "An integrated reduced inertial sensor system—RISS/GPS for land vehicle," in *2008 IEEE/ION Position, Location and Navigation Symposium*, 2008, pp. 1014–1021.

[37] J. Georgy, A. Noureldin, M. J. Korenberg, and M. M. Bayoumi, "Modeling the stochastic drift of a MEMS-based gyroscope in gyro/odometer/GPS integrated navigation," *IEEE Trans. Intell. Transp. Syst.*, vol. 11, no. 4, pp. 856–872, 2010.

[38] J. Georgy, T. Karamat, U. Iqbal, and A. Noureldin, "Enhanced MEMS-IMU/odometer/GPS integration using mixture particle filter," *GPS Solut.*, vol. 15, no. 3, pp. 239–252, 2011.

[39] M. A. Rashed, M. Elhabiby, U. Iqbal, M. J. Korenberg, and A. Noureldin, "Integration of Electronic Scanning Radars with Inertial Technology for Seamless Positioning in challenging GNSS Environments," in *2020 IEEE 92nd Vehicular Technology Conference (VTC2020-Fall)*, 2020, pp. 1–5.

[40] S. B. Azmy, N. Zorba, and H. S. Hassanein, "Robust quality metric for scarce mobile crowd-sensing scenarios," 2018, doi: 10.1109/ICCW.2018.8403744.

[41] S. B. Azmy, N. Zorba, and H. S. Hassanein, "Bootstrap-Based Quality Metric for Scarce Sensing Systems," 2018, doi: 10.1109/GLOCOM.2018.8647536.

[42] S. B. Azmy, R. A. Sneineh, N. Zorba, and H. S. Hassanein, "Small Data in IoT: An MCS Perspective," 2019.

[43] M. A. Fischler and R. C. Bolles, "Random sample consensus: A Paradigm for Model Fitting with Applications to Image Analysis and Automated Cartography," *Commun. ACM*, 1981, doi: 10.1145/358669.358692.

[44] R. Schnabel, R. Wahl, and R. Klein, "Efficient RANSAC for point-cloud shape detection," *Comput. Graph. Forum*, 2007, doi: 10.1111/j.1467-8659.2007.01016.x.

[45] S. Choi, T. Kim, and W. Yu, "Performance evaluation of RANSAC family," 2009, doi: 10.5244/C.23.81.

[46] U. Iqbal, A. F. Okou, and A. Noureldin, "An integrated reduced inertial sensor system - RISS / GPS for land vehicle," 2008, doi: 10.1109/PLANS.2008.4570075.

[47] S. Kaoud, A. Noureldin, and G. Fotopoulos, "Low-cost indoor vision-based navigation for mobile robots," Proceedings of the 33rd International Technical Meeting of the Satellite Division of the Institute of Navigation (ION GNSS+2020), 2020, pp. 2560-2568.

[48] S. Kaoud, "Vision-aided Intertial System for Near-real-time Positioning and Navigation of Unmanned Ground Survey Vehicles in GNSS-denied Environments," Master's thesis, Queen's University.

Marwan A. Rashed was born in Alexandria, Egypt in 1995. He received the B.S. degree in Mechanical Engineering from Arab Academy of Science and Technology (AAST), Alexandria, Egypt in 2017. He holds MSc degree in Electrical and Computer Engineering from Queen's University, Kingston, ON, Canada in 2019. He is currently a Research Assistant with the Navigation and Instrumentation Research Group (NAVINST), Royal Military College of Canada (RMCC). His research interests include Sensor Fusion, Autonomous and Vehicular localization, Robotic Ego-motion Estimation, Automotive Radar fusion, Machine Learning, Deep Learning and Machine Learning in Natural Language Processing.

Dr. Haidy Elghamrawy received her B.Sc. degree (2009) in Electronics and Communications Engineering from Cairo University, Cairo, Egypt. She received her M.Sc. degree (2013) in Engineering Mathematics and Physics from Cairo University and her Ph.D. degree (2019) from Queen's University, Kingston, Ontario, Canada. She is currently an Assistant Professor in the Department of Electrical and Computer Engineering at the Royal Military College of Canada (RMCC) and a Teaching Assistant at the Department of Engineering Mathematics and Physics, Faculty of Engineering, Cairo University, Egypt. Her research focuses on GNSS positioning, anti-jamming techniques, sensor fusion and autonomous driving systems.

Dr. Mohamed Elhabiby received both his Ph.D. in Geomatics Engineering in 2006 and Executive MBA with a finance major in 2017 from the University of Calgary. He is currently an Associate Professor, Public Works Department, Faculty of Engineering, Ain Shams, Cairo, Egypt. He published more than 120 academic journals, conference presentations, book Chapters, workshop proceedings and technical reports. He supervised several PhD, MSc. Students and Post Doctorate Fellows at both Academia and Industry. Dr. Elhabiby is goal-driven professional with strong R&D academic and industrial experience. He won the Alberta Science and Technology Foundation (ASTech) Award in Applied Technology 2015. He is named by Avenue Magazine as one of the Top 40 under 40 2013 class.

Michael J. Korenberg received the B.Sc. and M.Sc. degrees in mathematics and the Ph.D. degree in electrical engineering from McGill University, Montreal, QC, Canada.
He has been a Faculty Member at Queen's University since 1983, where he is currently a Professor with the Department of Electrical and Computer Engineering. His research interests include the development of practical methods for representing/identifying nonlinear systems of unknown structure and for time-series analysis. Applications relate to communications, to the modeling of physical and physiological processes, and to computational biology and bioinformatics. The latter applications include protein sequence classification, gene recognition, and interpretation of microarray data. For example, he has shown how nonlinear system identification techniques, such as parallel cascade identification can be used to classify protein sequences into structure or function families.

Dr. Aboelmagd Noureldin is a Senior member of IEEE and a professional member of the Institute of Navigation (ION). He holds B.Sc. degree in Electrical Engineering (1993) and M.Sc. degree in Engineering Physics (1997) both from Cairo University, Egypt. In addition, he holds Ph.D. degree in Electrical and Computer Engineering (2002) from The University of Calgary, Alberta, Canada. Since 2003, He has been a Professor at the Department of Electrical and Computer Engineering, Royal Military College of Canada with Cross-Appointment at both the School of Computing and the Department of Electrical and Computer Engineering, Queen's University. He published two books, 4 book chapters and over 270 papers in academic journals, conference, and workshop proceedings, in which he received several awards. He is also the director of the Navigation and Instrumentation (NavINST) research group at RMCC. He has been a leader in the field of inertial navigation, global navigation satellite systems including GPS, wireless location and navigation, intelligent multi-sensor systems with applications related to positioning and navigation of autonomous vehicles and mobile robot systems; machine learning-based human activity recognition and positioning; integrated wireless indoor navigation; intelligent transportation, and road information services.